

Is rhodium tetroxide in the formal oxidation state VIII stable? a quantum chemical and matrix isolation investigation of rhodium oxides

Yu Gong · Mingfei Zhou · Lester Andrews ·
Tobias Schlöder · Sebastian Riedel

Received: 7 December 2010 / Accepted: 7 March 2011 / Published online: 30 March 2011
© Springer-Verlag 2011

Abstract The structures and reactions of different rhodium oxides and dioxygen complexes with RhO_4 stoichiometry were investigated by matrix isolation infrared spectroscopy and quantum chemical calculations. The inserted RhO_2 molecule reacted with dioxygen upon sample annealing to form the $[(\eta^1\text{-O}_2)\text{RhO}_2]$ complex, which can further isomerize to the known $[(\eta^2\text{-O}_2)\text{RhO}_2]$ complex via infrared irradiation. Both experimental and theoretical studies suggest that the $[(\eta^1\text{-O}_2)\text{RhO}_2]$ complex has a doublet ground state with non-planar C_s symmetry in which the O_2 ligand is end-on bonded to the rhodium centre. Although rhodium tetroxide is predicted to be a stable molecule with D_{2d} symmetry at different level of

theory, no evidence is found for the formation of this $\text{Rh}(\text{VIII})$ species in noble gas matrices. Our experiments also suggest the formation of a new peroxy $[\text{Rh}(\eta^2\text{-O}_2)_2]$ complex, which is calculated to have a doublet ground state with D_{2d} symmetry. This peroxy complex undergoes isomerization to the known superoxo $[\text{Rh}(\eta^2\text{-O}_2)_2]$ complex via the rotation of the dioxygen ligand under infrared irradiation.

Keywords Rhodium oxides · Matrix isolation spectroscopy · Quantum chemical calculations · High oxidation states

1 Introduction

The highest experimentally found oxidation state of any chemical element is VIII. Apart from some xenon compounds, this oxidation state is represented by the well-known group 8 complexes HsO_4 , OsO_4 and RuO_4 and its derivatives [1–7]. In this case, the maximum oxidation state coincides with its group number 8 and thus with its valence electrons.

Very recently, we have experimentally shown that the formal oxidation state VIII can also be stabilized for elements placed on the right side of group 8 in the periodic table, particularly iridium [8]. Furthermore, quantum chemical calculations have predicted that the formal oxidation state IX can be stabilized for the group 9 elements (rhodium, iridium and meitnerium) in its cationic tetroxide complexes with a maximal stability for the $[\text{IrO}_4]^+$ cation [9].

The IrO_4 molecule has been prepared by the reactions of iridium atoms with dioxygen in solid noble gas matrixes [8]. Iridium atoms insert into dioxygen to form the iridium

Dedicated to Professor Pekka Pyykkö on the occasion of his 70th birthday and published as part of the Pyykkö Festschrift Issue.

Electronic supplementary material The online version of this article (doi:[10.1007/s00214-011-0919-7](https://doi.org/10.1007/s00214-011-0919-7)) contains supplementary material, which is available to authorized users.

Y. Gong · M. Zhou
Department of Chemistry, Shanghai Key Laboratory of Molecular Catalysts and Innovative Materials, Advanced Materials Laboratory, Fudan University, 200433 Shanghai, China
e-mail: mfzhou@fudan.edu.cn

L. Andrews
Department of Chemistry, University of Virginia, Charlottesville, VA 22904-4319, USA

T. Schlöder · S. Riedel (✉)
Institut für Anorganische und Analytische Chemie, Albert-Ludwigs Universität Freiburg, Albertstrasse 21, 79104 Freiburg i. Br., Germany
e-mail: sriedel@psichem.de

dioxide molecules. Annealing supported the formation of the iridium dioxide superoxide complex $[(\eta^1\text{-O}_2)\text{IrO}_2]$, which isomerizes under the IR irradiation to the iridium dioxide peroxide complex $[(\eta^2\text{-O}_2)\text{IrO}_2]$. These complexes photochemically rearrange to the iridium tetroxide molecule with a formal iridium oxidation state of VIII. After these experimental findings, one question remains unanswered: is the lighter homologue of the iridium tetroxide, namely rhodium tetroxide, also stable? A stability of this molecule would be in line with the group 8 oxides OsO_4 and RuO_4 , see above.

Herein, we report a combined matrix isolation spectroscopic and theoretical study of rhodium oxides and dioxygen complexes with RhO_4 stoichiometry. To put these data into perspective, a comparison with its heavier homologue iridium is made.

2 Experimental and computational methods

2.1 Experimental methods

The experimental set-up for pulsed laser evaporation and matrix isolation infrared spectroscopic investigation has been described in detail previously [10]. Briefly, the 1,064 nm fundamental of a Nd:YAG laser (Continuum, Minilite II, 10 Hz repetition rate and 6 ns pulse width) was focused onto a rotating rhodium target through a hole in a CsI window cooled normally to 6 K(Ar) or 4 K(He) by means of a closed-cycle helium refrigerator. The laser-evaporated metal atoms were codeposited with O_2/Ar or O_2/Ne mixtures onto the CsI window. In general, matrix samples were deposited for 1 h (Ar) or 0.5 h (Ne) at a rate of approximately 4 mmol/h. The O_2/Ar and O_2/Ne mixtures were prepared in a stainless steel vacuum line using standard manometric technique. Isotopic $^{18}\text{O}_2$ (ISOTEC, 99%) was used without further purification. The scrambled $^{16}\text{O}_2 + ^{16}\text{O}^{18}\text{O} + ^{18}\text{O}_2$ mixture was prepared via Tesla coil discharge of the mixed $^{16}\text{O}_2 + ^{18}\text{O}_2$ (1:1) sample. The infrared absorption spectra of the resulting samples were recorded on a Bruker IFS 66 V and Vertex 80 V spectrometers at 0.5 cm^{-1} resolution between 4,000 and 450 cm^{-1} using a liquid nitrogen-cooled HgCdTe (MCT) detector. Samples were annealed in the dark (out of the spectrometer beam line) to different temperatures and cooled back to 6 or 4 K for spectral acquisition. Selected samples were subjected to broad band irradiation using a tungsten lamp or a high-pressure mercury arc lamp with glass filters. Typically, the infrared spectra were recorded with 150–200 scans, but only 10 or 20 scans were employed in some cases due to the infrared-induced decrease in the product absorptions.

2.2 Calculations

All structures of the considered molecules have been optimized at DFT level using the B3LYP hybrid functional (based on the work of Becke) [11] and the triple- ζ correlation consistent basis sets aug-cc-pVTZ-PP and aug-cc-pVTZ for rhodium and oxygen [12], respectively. Energy gaps between different spin states have been evaluated by B3LYP, BP86 and M052X density functionals, see Supporting Information Table S1. Scalar relativistic effects for Rh were included by a quasirelativistic energy-adjusted, small-core pseudopotential (effective-core potential, ECP) [13]. All DFT calculations have been performed with the Gaussian 03 Rev. E.01 program package [14].

Stationary points on the potential energy surface have been characterized by harmonic as well as anharmonic frequency analyses. Also, isotopic shifts have been calculated for the all- ^{16}O and all- ^{18}O isotopomers. The relaxed potential energy scans as well as the optimization of the transition state structure have been performed by using standard procedure implemented in the Gaussian 03 program.

The coupled-cluster calculations with single and double excitations (CCSD), as well as with inclusion of perturbative triple excitations [CCSD(T) level], were carried out with the MOLPRO 2006 program package [15]. CCSD(T) single-point calculations at B3LYP-optimized structures have been performed using different correlation consistent basis set qualities of oxygen [aug-cc-pVQZ (X = D, T, Q)] [12]. We note that the methodology used here, in particular B3LYP optimizations followed CCSD(T) single-point energy calculations with larger basis sets, is well established as a reliable tool for redox thermochemistry in the 5d transition metal series, for example in previous studies on Hg, Au, Pt and Ir systems [16–20].

Our recent investigation on spin-orbit (SO) coupling of group 9 tetroxide complexes shows only minor effects on the stability of the rhodium and iridium species, whereas SO coupling increases enormously for the corresponding Eka-Iridium (Meitnerium) complexes and destabilizes these [9]. Therefore, we have not investigated the SO coupling of rhodium oxide species.

Note, in case of our coupled-cluster calculations on single-point B3LYP structures, we observed relatively high T_1 -diagnostic [21] values of the $[(\eta^1\text{-O}_2)\text{RhO}_2]$ complex in both electron configurations, doublet 0.053 and quartet 0.090 whereas the highest T_2 amplitudes are below 0.15: doublet $|T_2(\max)|$ 0.1083 and quartet $|T_2(\max)|$ 0.0572. This indicates that the occurring behaviour is not due to “multireference” character of the wave function but rather a problem of spin contamination. In case of the RhO_2 , we have observed normal values of (doublet T_1 -diagnostic:

0.0423, $|T_2(\text{max})| = 0.0995$), which is in contrast with the isovalent $[\text{FeO}_2]^-$ [22].

3 Results and discussions

3.1 Infrared spectra

Figure 1 shows the infrared spectra in selected regions from codeposition of laser-evaporated rhodium atoms with 0.5% O_2 in argon. In addition to the O_4^- anion absorption at 953.8 cm^{-1} (not shown in Fig. 1) [23], the spectrum after sample deposition is dominated by the rhodium dioxide (RhO_2) absorption at 899.9 cm^{-1} (Fig. 1, trace a) [24]. The weak band at 893.6 cm^{-1} was recently assigned to the antisymmetric ORhO stretching vibration of rhodium dioxide anion [25]. Broad band irradiation with the output of a high-pressure mercury arc lamp ($250 < \lambda < 580 \text{ nm}$) destroyed the anion absorptions while the RhO_2 absorption increased. Three absorptions at $1,116.5$, 890.6 and 837.7 cm^{-1} (labelled 1 in Fig. 1) increased at the cost of RhO_2 absorption during subsequent sample annealing (Fig. 1, trace c). All these bands decreased when the sample was exposed to the infrared light ($7,500\text{--}370 \text{ cm}^{-1}$) from the source of the spectrometer. At the same time, another three bands at 928.6 , 865.0 and 831.1 cm^{-1} (labelled 2 in Fig. 1) appeared, which were previously assigned to the side-on bonded $[(\eta^2\text{-O}_2)\text{RhO}_2]$ molecule

[24]. Further near-infrared irradiation ($\lambda > 850 \text{ nm}$) completely destroyed the $[(\eta^2\text{-O}_2)\text{RhO}_2]$ absorptions while the $1,116.5$, 890.6 and 837.7 cm^{-1} absorptions increased again (Fig. 1, trace e). No new product absorption was produced when the sample was irradiated with UV and visible light (Fig. 1, traces f, g).

The infrared spectra from reactions of rhodium atoms and 0.5% O_2 in argon but with lower laser energy are shown in Fig. 2. Obviously, rhodium dioxide absorption is barely observed upon sample deposition due to the lack of excited rhodium atoms during ablation process (Fig. 2, trace a). When the sample was annealed right after deposition, absorptions at $1,116.5$, 890.6 and 837.7 cm^{-1} were produced but with lower intensities. The major absorptions after sample annealing appeared at $1,048.4$ (labelled A in Fig. 2), 959.5 (not shown in Fig. 2), 922.3 and 551.8 cm^{-1} (labelled B in Figs. 1, 2). All of these four bands were also observed in Fig. 1. The $1,048.4$ and 959.5 cm^{-1} absorptions were recently assigned to the O–O stretching vibrations of the $[\text{Rh}(\eta^2\text{-O}_2)_2]$ and $[\text{Rh}(\eta^2\text{-O}_2)]$ complexes, respectively [26], while group B absorptions are still unknown. As shown in Figs. 2 and 3, group B absorptions are sensitive to the infrared light from the source, and infrared irradiation induced the conversion from B to A. Subsequent visible irradiation reproduced group B absorptions with a slightly decrease in group A absorption.

Experiments were repeated using isotopic substituted $^{18}\text{O}_2$, $^{16}\text{O}_2 + ^{18}\text{O}_2$ (1:1) and $^{16}\text{O}_2 + ^{16}\text{O}^{18}\text{O} + ^{18}\text{O}_2$ (1:2:1) mixtures to help product identifications. The spectra in selected regions with different isotopic samples are shown

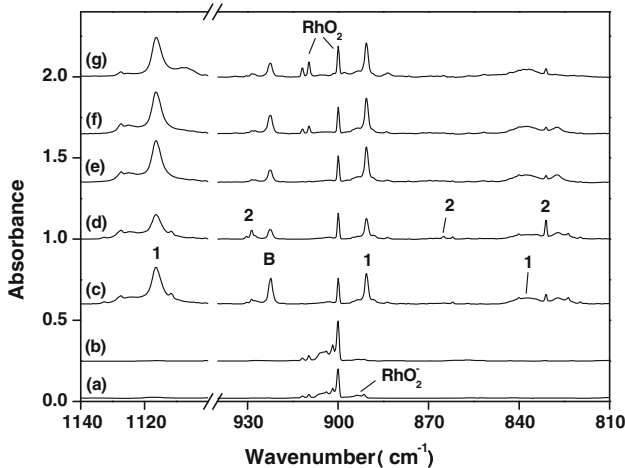


Fig. 1 Infrared spectra in the $1,140\text{--}1,100$ and $940\text{--}810 \text{ cm}^{-1}$ regions from codeposition of laser-evaporated rhodium atoms with 0.5% O_2 in argon (high laser energy). *a* 1 h of sample deposition at 6 K, *b* after 10 min of broad band irradiation ($250 < \lambda < 580 \text{ nm}$), *c* after annealing to 35 K, 10 scans, *d* after 10 min of infrared irradiation from the source, *e* after 10 min of $\lambda > 850 \text{ nm}$ irradiation, 10 scans, *f* after 10 min of $\lambda > 500 \text{ nm}$ irradiation, 10 scans and *g* after 10 min of $250 < \lambda < 580 \text{ nm}$ irradiation, 10 scans. Labels 1 and 2 denote the absorptions of the $[(\eta^1\text{-O}_2)\text{RhO}_2]$ and $[(\eta^2\text{-O}_2)\text{RhO}_2]$ complexes. All the samples were annealed in the dark

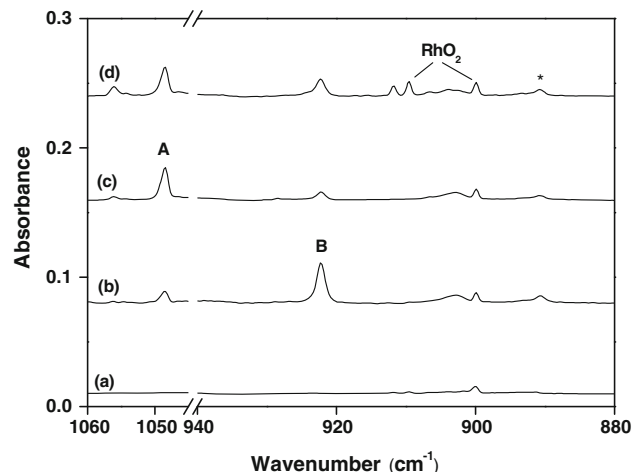


Fig. 2 Infrared spectra in the $1,060\text{--}1,045$ and $940\text{--}880 \text{ cm}^{-1}$ regions from codeposition of laser-evaporated rhodium atoms with 0.5% O_2 in argon (low laser energy). *a* 1 h of sample deposition at 6 K, *b* after annealing to 25 K, 10 scans, *c* after 10 min of infrared irradiation from the source and *d* after 10 min of $\lambda > 500 \text{ nm}$ irradiation, 10 scans. The asterisk denotes the absorption of the $[(\eta^1\text{-O}_2)\text{RhO}_2]$ complex. All the samples were annealed in the dark

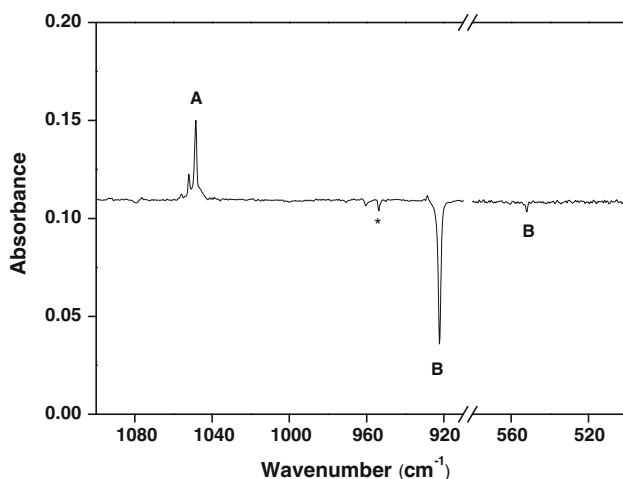


Fig. 3 Difference IR spectrum in the 1,100–910 and 580–500 cm^{-1} regions from codeposition of laser-evaporated rhodium atoms with 0.5% O_2 in argon (Spectrum taken after 20 min of infrared irradiation from the source (200 scans) minus spectrum taken right after 25 K annealing (10 scans)). The asterisk denotes the absorption of O_4^- anion

in Figs. 4 and 5 with the band positions of the product absorptions listed in Table 1.

All the above-mentioned products were also observed in the experiments performed in neon matrix (Fig. 6), and their band positions are listed in Table 2. Note that the neon-to-argon shifts for most molecules are less than 10 cm^{-1} , suggesting weak interactions between guest molecules and host matrix atoms [27]. The large shift for

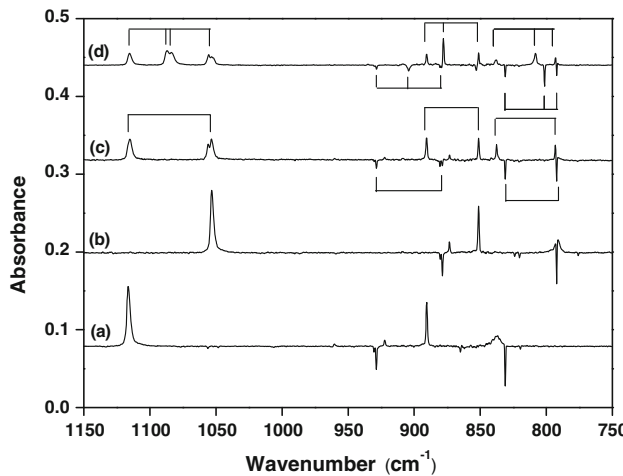


Fig. 4 Difference IR spectrum in the 1,150–750 cm^{-1} region from codeposition of laser-evaporated rhodium atoms with different isotopic samples in argon (Spectrum taken after 10 min of infrared irradiation from the source (200 scans) minus spectrum taken right after $\lambda > 850$ nm irradiation (10 scans)). *a* 0.5% $^{16}\text{O}_2$, *b* 0.5% $^{18}\text{O}_2$, *c* 0.25% $^{16}\text{O}_2 + 0.25\%$ $^{18}\text{O}_2$ and *d* 0.125% $^{16}\text{O}_2 + 0.25\%$ $^{16}\text{O}^{18}\text{O} + 0.125\%$ $^{18}\text{O}_2$. Bands upward denote the absorptions of $[(\eta^1-\text{O}_2)\text{RhO}_2]$, and bands downward denote the absorptions of $[(\eta^2-\text{O}_2)_2]$

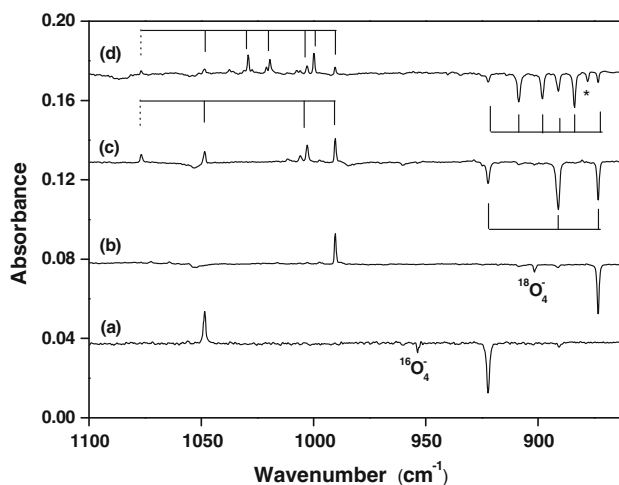


Fig. 5 Difference IR spectrum in the 1,100–860 cm^{-1} region from codeposition of laser-evaporated rhodium atoms with different isotopic samples in argon (Spectrum taken after 20 min of infrared irradiation from the source (200 scans) minus spectrum taken right after 25 K annealing (10 scans)). *a* 0.5% $^{16}\text{O}_2$, *b* 0.5% $^{18}\text{O}_2$, *c* 0.25% $^{16}\text{O}_2 + 0.25\%$ $^{18}\text{O}_2$ and *d* 0.125% $^{16}\text{O}_2 + 0.25\%$ $^{16}\text{O}^{18}\text{O} + 0.125\%$ $^{18}\text{O}_2$. Bands upward denote the absorptions of $[\text{Rh}(\eta^2-\text{O}_2)_2]$ (A), and bands downward denote the absorptions of $[\text{Rh}(\eta^2-\text{O}_2)_2]$ (B). The asterisk denotes the absorption of the $[(\eta^1-\text{O}_2)\text{RhO}_2]$ complex

the $[\text{Rh}(\eta^2-\text{O}_2)]$ complex is due to the coordination of argon atoms to the rhodium centre in argon matrix [26].

3.2 $[(\eta^1-\text{O}_2)\text{RhO}_2]$

The 1,116.5, 890.6 and 837.7 cm^{-1} absorptions increased together on annealing, and they were interconvertible with the $[(\eta^2-\text{O}_2)\text{RhO}_2]$ molecule under different infrared irradiation. The formation of these bands was favoured only when the RhO_2 absorption was strong. All these observations suggest that the 1,116.5, 890.6 and 837.7 cm^{-1} absorptions should be due to a new isomer of the $[(\eta^2-\text{O}_2)\text{RhO}_2]$ complex. The first two bands were observed previously but remained unidentified [24]. With our well-resolved infrared spectra, we can determine the structure of this molecule. The 1,116.5 cm^{-1} absorption shifted to 1,053.2 cm^{-1} with $^{16}\text{O}/^{18}\text{O}$ ratio of a typical O–O vibration. Two doublets at 1,116.5, 1,115.0, 1,055.9 and 1,053.3 cm^{-1} were observed in the mixed $^{16}\text{O}_2 + ^{18}\text{O}_2$ (1:1) experiment (Fig. 4, trace c), suggesting the involvement of one O_2 molecule in this mode but slightly perturbed by another fragment. In the experiment with $^{16}\text{O}_2 + ^{16}\text{O}^{18}\text{O} + ^{18}\text{O}_2$ (1:2:1) sample, the intermediate absorption split into two closely spaced bands, which clearly indicated the two oxygen atoms are not equivalent (Fig. 4, trace d). For the other two bands at 890.6 and 837.7 cm^{-1} , they were, respectively, characterized as antisymmetric and symmetric ORhO stretching vibrations on the basis of $^{16}\text{O}/^{18}\text{O}$ ratio. Mixed isotopic experiments revealed that

Table 1 Infrared absorptions (cm^{-1}) of rhodium oxide species in solid argon

	$^{16}\text{O}_2$	$^{18}\text{O}_2$	$^{16}\text{O}_2 + ^{18}\text{O}_2$	$^{16}\text{O}_2 + ^{16}\text{O}^{18}\text{O} + ^{18}\text{O}_2$	Mode
$[(\eta^1\text{-O}_2)\text{RhO}_2]$	1,116.5	1,053.2	1,116.5, 1,115.0	1,115.4, 1,087.0,	O–O str.
			1,055.9, 1,053.3	1,083.6, 1,055.6, 1,053.3	
	890.6	851.3	890.6, 851.3	890.6, 877.9, 851.3	ORhO antisym. str.
$[(\eta^2\text{-O}_2)\text{RhO}_2]$	837.7	792.1	837.7, 793.1	837.7, 808.3, 792.8	ORhO sym str.
	928.6	878.7	928.6, 878.7	928.6, 904.2,... ^a	O–O str.
	865.0	820.3	865.0, 820.3	964.9, 852.9, 820.6	ORhO sym. str.
$[\text{Rh}(\eta^2\text{-O}_2)]$	831.1	792.1	831.1, 792.1	831.1, 801.3, 792.1	ORhO antisym. str.
	959.5	907.9	959.5, 907.9	959.5, 934.4, 907.9	O–O str.
	1,048.4	990.3	1,076.7, 1,048.4,	1,076.7, 1,048.4, 1,029.1,	O–O str.
$[\text{Rh}(\eta^2\text{-O}_2)_2]$ (A)			1,002.8, 990.3,	1,019.5, 1,002.8, 999.9,	
				990.3	
	922.3	873.3	922.3, 891.1, 873.3	922.3, 908.5, 898.1,	O–O str.
$[\text{Rh}(\eta^2\text{-O}_2)_2]$ (B)	551.8	531.3	551.8, 542.6, 531.8	551.8, 547.0, 542.1 ^a ,	Rh-(O_2) ₂ str.
				536.8, 531.3	
	911.7	872.3	911.7, 872.3	911.7, 899.9,	ORhO antisym. str.
RhO_2				872.3, 831.2	(site)
	909.6	870.2	909.6, 870.2	909.6, 897.8,	ORhO antisym. str.
				870.2, 829.4	(site)
$[\text{RhO}_2]^-$	899.9	861.1	899.9, 861.1	899.9, 888.0, 861.1	ORhO antisym. str.
	893.6	855.3	893.6, 855.3	... ^a , 877.6, 855.3	ORhO antisym. str.
	891.4	853.1	891.4, 853.1		ORhO antisym. str. (site)
RhO	799.0	759.8	799.0, 759.8	799.0, 759.8	RhO str.

^a Absorptions unresolved due to band overlap

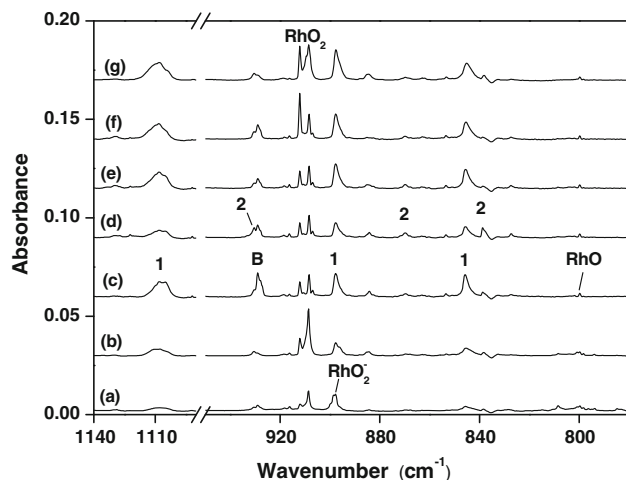


Fig. 6 Infrared spectra in the 1,140–1,090 and 950–780 cm^{-1} regions from codeposition of laser-evaporated rhodium atoms with 0.1% O_2 in neon. *a* 0.5 h of sample deposition at 4 K, *b* after 10 min of broad band irradiation ($250 < \lambda < 580 \text{ nm}$), *c* after annealing to 11 K, 20 scans, *d* after 10 min of infrared irradiation from the source, *e* after 10 min of $\lambda > 850 \text{ nm}$ irradiation, 20 scans, *f* after 10 min of $\lambda > 500 \text{ nm}$ irradiation, 20 scans and *g* after 10 min of $250 < \lambda < 580 \text{ nm}$ irradiation, 50 scans. Labels 1 and 2 denote the absorptions of $[(\eta^1\text{-O}_2)\text{RhO}_2]$ and $[(\eta^2\text{-O}_2)\text{RhO}_2]$ complexes. All the samples were annealed in the dark

Table 2 Infrared absorptions (cm^{-1}) of rhodium oxide species in solid neon

	$^{16}\text{O}_2$	$^{18}\text{O}_2$	Mode
$[(\eta^1\text{-O}_2)\text{RhO}_2]$	1,108.0	1,045.4	O–O str.
	897.7	858.1	ORhO antisym. str.
	845.7	799.8	ORhO sym str.
$[(\eta^2\text{-O}_2)\text{RhO}_2]$	930.4	880.1	O–O str.
	869.7	826.7	ORhO sym. str.
	838.8	799.6	ORhO antisym. str.
$[\text{Rh}(\eta^2\text{-O}_2)]$	975.8	923.1	O–O str.
$[\text{Rh}(\eta^2\text{-O}_2)_2]$ (A)	1,047.4	989.2	O–O str.
$[\text{Rh}(\eta^2\text{-O}_2)_2]$ (B)	929.1	879.6	O–O str.
RhO_2	912.1	872.7	ORhO antisym. str. (site)
	908.6	869.5	ORhO antisym. str.
$[\text{RhO}_2]^-$	898.6	859.9	ORhO antisym. str.
	897.7	859.2	ORhO antisym. str. (site)
RhO	799.8	760.8	RhO str.

only one RhO_2 fragment is involved in these modes. Accordingly, the three absorptions at 1,116.5, 890.6 and 837.7 cm^{-1} are assigned to the $[(\eta^1\text{-O}_2)\text{RhO}_2]$ complex, in

which the O₂ molecule is end-on bonded to the rhodium centre.

3.3 [Rh(η^2 -O₂)₂] (B)

As shown in Figs. 2 and 3, the 922.3 and 551.8 cm⁻¹ (B) absorptions are interconvertible with the previously identified bis-superoxo [Rh(η^2 -O₂)₂] complex (A) [26]. The ¹⁶O/¹⁸O ratio for the 922.3 cm⁻¹ absorption characterizes an O–O stretching vibration. A similar pattern with the known [Rh(η^2 -O₂)₂] complex (A) was observed for the 922.3 cm⁻¹ absorption in the mixed ¹⁶O₂ + ¹⁸O₂ (1:1) and ¹⁶O₂ + ¹⁶O¹⁸O + ¹⁸O₂ (1:2:1) experiments (Fig. 5), indicating that group B absorptions should be a rhodium bis-dioxygen complex as well. The weak band at 551.8 cm⁻¹ is due to a Rh-(O₂)₂ vibration. It can be found in Figs. 1 and 2 that the formation of the 922.3 and 551.8 cm⁻¹ absorptions is independent of rhodium dioxide, and no ORhO stretching vibration was observed to track these two bands. Hence, we assign the 922.3 and 551.8 cm⁻¹ absorptions to the [Rh(η^2 -O₂)₂] complex (B). The new [Rh(η^2 -O₂)₂] complex (B) identified here can be regarded as a peroxy complex on the basis of its O–O vibrational frequency [28], which is different from the superoxo [Rh(η^2 -O₂)₂] complex (A) [26].

3.4 Quantum chemical calculations

All isomers of rhodium oxides and dioxygen complexes with RhO₄ stoichiometry have been quantum chemically investigated. The optimized structures are shown in Fig. 7, and the calculated thermochemistry and vibrational frequencies at DFT and coupled-cluster level are shown in Tables 3, 4, 5, 6. The [(η^2 -O₂)RhO₂] isomer is formed via

reaction between the inserted rhodium dioxide and dioxygen under cryogenic conditions and characterized by its IR bands in the matrix isolation experiment, see Fig. 1 Label 2 and ref. [24]. The species is predicted to have C_{2v} symmetry with an electron configuration of ²A₂ which is in agreement with previous investigations [24]. The doublet configuration has been calculated to be the ground state at different levels of theory with the exception of the M05-2X functional which leads to a quartet state lying 9.2 kJ mol⁻¹ lower in energy (see Table S1). The side-on bonded peroxy group has been computed to be 139.7 and 140.6 pm long at B3LYP and CCSD(T) level, respectively. This is slightly shorter than the peroxy bond found in [$(\eta^2$ -O₂)IrO₂] of 142.8 pm at B3LYP and 145.1 pm at CCSD(T) level [8]. Our calculated harmonic frequencies are consistently shifted to higher wavenumbers if compared with the experimental absorption bands, see Table 4. If we take anharmonic corrections into account, the agreement improves slightly. This difference between the experimental and computed wavenumbers is at one side due to the used quantum chemical level, in this case DFT, and on the other side due to the experimental matrix shift (influence of the noble gas matrix to the guest species) which is still neglected by our calculations. Nevertheless, isotopic labelling of the species in question with ¹⁶O and ¹⁸O allows the right assignment of the observed bands. The isotopic shifts of the experimental and calculated anharmonic O–O stretch (a₁) 49.9/45.4 cm⁻¹, ORhO symmetric stretch (a₁) 44.7/48.8 cm⁻¹ and the ORhO antisymmetric stretch (b₁) 39.0/40.5 cm⁻¹ are in good agreement, see Table 4.

The [(η^1 -O₂)RhO₂] isomer with an end-on coordinated superoxide ligand is 30.3 kJ/mol higher in energy than the side-on bonded peroxy complex at DFT level (Fig. 8).

Fig. 7 B3LYP-optimized structures of rhodium oxide molecules. The doublet and quartet state of [$(\eta^1$ -O₂)RhO₂] and [Rh(η^2 -O₂)₂] are shown. **a** RhO₂ (point group C_{2v}, electronic state: ²A₁), **b** [RhO₂]⁻ (C_{2v}, ¹A₁), **c** Rh(η^2 -O₂) (C_{2v}, ²A₂), **d** [$(\eta^1$ -O₂) RhO₂] (C_s, ²A'), **e** [$(\eta^1$ -O₂)RhO₂] (C_s, ⁴A'), **f** [Rh(η^2 -O₂)₂] (D_{2d}, ²B₁), **g** [Rh(η^2 -O₂)₂] (D_{2h}, ⁴B_{1u}), **h** [$(\eta^2$ -O₂)RhO₂] (C_{2v}, ²A₂) and **i** RhO₄ (D_{2d}, ²A₁)

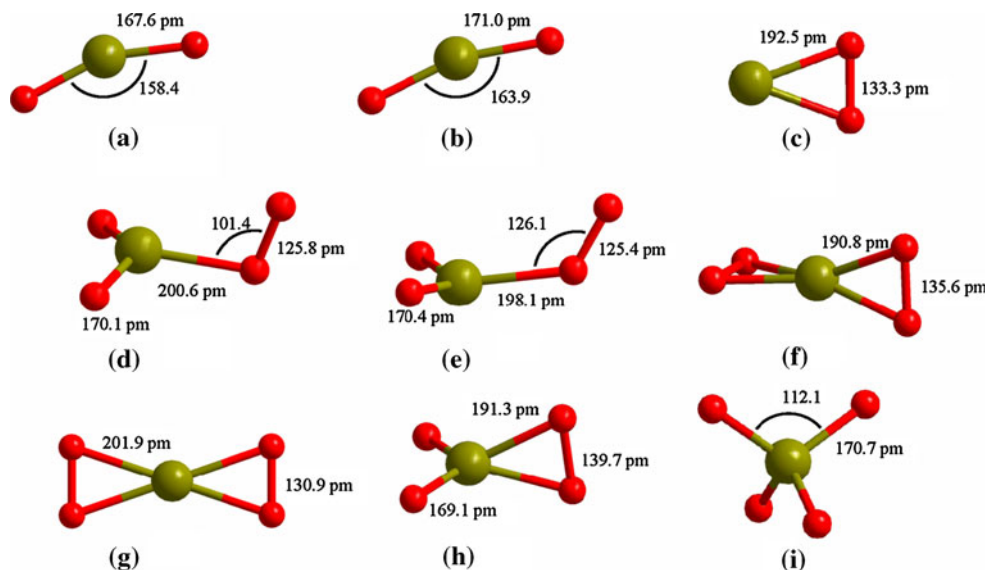


Table 3 Thermochemistry of RhO_4 and RhO_2 isomers at different levels of theory in [kJ mol⁻¹]

Reaction	B3LYP	BP86	M05-2X	CCSD(T)			
	OPT ^{a,b}	OPT ^{c,b}	OPT ^{d,b}	OPT ^e	SP/DZ ^f	SP/TZ ^f	SP/QZ ^f
a. $\text{RhO}_4 \rightarrow [\eta^2\text{-O}_2]\text{RhO}_2$	-47.9 (-49.4)	18.4 (17.5)	-141.1 (-142.6)	-25.7	-9.9	-26.7	-26.2
b. $\text{RhO}_4 \rightarrow [\eta^1\text{-O}_2]\text{RhO}_2$ ^g	-17.6 (-21.5)	56.8 (54.1)	-98.2 (-100.3)		83.3	69.6	71.5
c. $\text{RhO}_4 \rightarrow \text{Rh}(\eta^2\text{-O}_2)_2$ ^h	-15.5 (-17.8)	134.9 (132.6)	-225.3 (-226.2)		78.1	50.8	54.0
d. $\text{RhO}_4 \rightarrow \text{RhO}_2 + \text{O}_2$	-35.2 (-42.6)	104.0 (96.8)	-154.5 (-161.9)	-5.8	7.1	-4.0	-0.6
e. $[\eta^1\text{-O}_2]\text{RhO}_2 \rightarrow \text{RhO}_2 + \text{O}_2$	-17.5 (-21.1)	47.2 (42.7)	-56.2 (-61.6)		-76.2	-73.9	-72.1
f. $[\eta^2\text{-O}_2]\text{RhO}_2 \rightarrow \text{RhO}_2 + \text{O}_2$	12.7 (6.8)	85.6 (79.4)	-13.3 (-19.3)	19.9	17.0	22.7	25.7
g. $\text{Rh}(\eta^2\text{-O}_2)_2 \rightarrow \text{Rh}(\eta^2\text{-O}_2) + \text{O}_2$	165.1 (157.9)	196.9 (190.8)	177.0 (169.1)		165.8	158.9	159.0
h. $\text{Rh}(\eta^2\text{-O}_2)_2 \rightarrow \text{RhO}_2 + \text{O}_2$	-19.7 (-24.8)	-30.8 (-35.7)	70.8 (64.4)		-70.9	-54.8	-54.5
i. $\text{RhO}_2 \rightarrow \text{Rh} + \text{O}_2$	297.2 (294.3)	428.1 (425.1)	218.4 (215.4)		364.1	347.3	352.6
j. $\text{RhO}_2 \rightarrow \text{Rh}(\eta^2\text{-O}_2)$	184.7 (182.7)	227.8 (226.6)	106.1 (104.8)		236.7	213.8	213.5

^a Thermochemistry at B3LYP/Rh:aug-cc-pVTZ-PP; O:aug-cc-pVTZ level, ^b Values in parenthesis are ZPE corrected. ^c Thermochemistry at BP86/Rh:aug-cc-pVTZ-PP; O:aug-cc-pVTZ level ^d Thermochemistry at M05-2X/Rh:aug-cc-pVTZ-PP; O:aug-cc-pVTZ level; ^e Optimizations at CCSD(T)/Rh:RSC-PP; O:aug-cc-pVTZ level. ^f Single-point calculations on B3LYP-optimized structures at CCSD(T)/Rh:aug-cc-pVTZ-PP; O:aug-cc-pVQZ X = D, T, Q level. ^g Doublet, ^h Quartet

The electron configuration of the minimum structure of this species is difficult to assign because the energy gap between the doublet ${}^2\text{A}'$ and the quartet ${}^4\text{A}'$ states is only 3.7 kJ/mol at B3LYP level with the quartet state being lower in energy. Other functionals such as BP86 and M05-2X show the doublet configuration to be the ground state (Table S1). In a previous investigation of rhodium oxide species using the GGA (generalized gradient approximation) functional BPW91, the doublet state was found to be 4 kJ/mol lower in energy [24]. This discrepancy of the spin-state splitting using different kinds of DFT functionals is known; for example pure functionals like LDA and GGA e.g. BPW91 systematically overestimate the stability of low-spin states whereas hybrid functionals like B3LYP or PBE overestimate the stability of high-spin states due to their inclusion of Hartree–Fock exchange [29, 30]. The comparison of the experimental isotopic shift with the calculated one shows an appropriate agreement for the ${}^2\text{A}'$ state, indicating that the doublet is indeed the lowest energy configuration of the $[(\eta^1\text{-O}_2)\text{RhO}_2]$ complex, see Table 4. The experimental and calculated isotopic shifts of the ^{16}O and ^{18}O are O–O stretch (a') 63.3/72.4 cm⁻¹, ORhO antisymmetric stretch (a'') 39.3/42.2 cm⁻¹ and the ORhO symmetric stretch (a') 45.6/38.9 cm⁻¹. Furthermore, the relative intensities of these three modes for the doublet complex are in better agreement with the experimental infrared intensities, which also provide support to the assignment of the ${}^2\text{A}'$ ground state of the $[(\eta^1\text{-O}_2)\text{RhO}_2]$ molecule.

Calculations of the $[\text{Rh}(\eta^2\text{-O}_2)_2]$ complex as doublet and quartet states show D_{2d} and D_{2h} symmetry, respectively, see Fig. 7. The latter is experimentally known from its absorption at 1,048.4 cm⁻¹ and is characterized to be a bis-superoxide complex with a ground-state electron configuration of ${}^4\text{B}_{1u}$ which is 12.6 kJ/mol lower in energy than the new D_{2d} peroxy

complex, see Fig. 9. The energy gap between the two molecules depends strongly on the used method (Table S1). The M05-2X functional overestimates the stability of the quartet state whereas BP86 does so for the doublet configuration; both B3LYP and single-point CCSD(T) calculations show very small energy gaps. Note, the single-point CCSD(T) calculations have been carried out on B3LYP-optimized structures and might not represent the ideal symmetry of the molecule as BP86 shows a distortion from D_{2h} symmetry for the quartet state. The experimental finding of both species corroborates the small energetic differences between the two molecules. The new band at 922.3 cm⁻¹ is due to the only observed O–O stretching vibrational mode of the peroxy complex (B). The optimized structure shows a D_{2d} symmetry with an electron configuration of ${}^2\text{B}_1$. Its O–O bond length is 5 pm longer than that of the superoxo complex and is thus more close to the O–O bond length of the hydrogen peroxide (experimental gas-phase structure, 147.5 pm [5]), see Fig. 7. Our calculated isotopic shift is in agreement with the experimental observation (Table 5): antisymmetric O–O stretch (b_2) 49.0/53.1 cm⁻¹ and Rh-(O₂)₂ antisymmetric stretch (b_2) 20.5/21.6 cm⁻¹. Both species are interconvertible by rotation of the peroxide bond as indicated by the observed bands, see Figs. 2 and 3. This process was investigated by a relaxed potential energy surface (PES) scan at B3LYP level of the doublet and quartet states of $[\text{Rh}(\eta^2\text{-O}_2)_2]$, see Fig. 9. The point of spin-crossover is reached at an angle between 50° and 55°. This rough interpretation of the photolytically initiated interconversion process between these two states allows the estimation of the ‘barrier’ which is approximately 80 kJ/mol high.

The open-shell (d^1) RhO_4 isomer exhibits moderate Jahn–Teller distortion from a regular tetrahedron to D_{2d} symmetry. Its bond length is computed to be 170.7 and 171.9 pm at B3LYP and CCSD(T) level, respectively, see

Table 4 Experimental (in argon matrix) and calculated wavenumbers and isotopic shifts for $[(\eta^1\text{-O}_2)\text{RhO}_2]$ and $[(\eta^2\text{-O}_2)\text{RhO}_2]$; all values in cm^{-1}

Molecule	Mode		Exp.	Calc. ^{a,b}	Rel. Int. ^b	Calc. ^{a,c}	Ref.
$[(\eta^1\text{-O}_2)\text{RhO}_2]$ $^2\text{A}'$	O–O str. (a')	$\tilde{\nu}$ (Rh^{16}O_2)	1,116.5	1,296.8/1,285.3	100	1,061.1/1,050.3	This paper
		$\tilde{\nu}$ (Rh^{18}O_2)	1,053.2	1,222.5/1,212.9		1,000.0/978.2	
		$\Delta\tilde{\nu}$	63.3	74.3/72.4		61.1/72.1	
	ORhO antisym. str. (a'')	$\tilde{\nu}$ (Rh^{16}O_2)	890.6	938.9/931.6	83	893.7/873.3	
		$\tilde{\nu}$ (Rh^{18}O_2)	851.3	896.4/889.4		852.8/829.3	
		$\Delta\tilde{\nu}$	39.3	42.5/42.2		40.9/44.0	
	ORhO sym. str. (a')	$\tilde{\nu}$ (Rh^{16}O_2)	837.7	903.3/891.6	12	865.1/851.4	
		$\tilde{\nu}$ (Rh^{18}O_2)	792.1	854.6/844.2		818.3/802.1	
		$\Delta\tilde{\nu}$	45.6	48.7/47.4		46.8/49.3	
$[(\eta^1\text{-O}_2)\text{RhO}_2]$ $^4\text{A}'$	O–O str. (a')	$\tilde{\nu}$ (Rh^{16}O_2)	1,116.5	1,227.8/1,208.4	100	1,221.0/1,204.6	
		$\tilde{\nu}$ (Rh^{18}O_2)	1,053.2	1,157.6/1,140.0		1,151.0/1,135.5	
		$\Delta\tilde{\nu}$	63.3	70.2/68.4		70.0/69.1	
	ORhO antisym. str. (a'')	$\tilde{\nu}$ (Rh^{16}O_2)	890.6	910.1/897.7	1	851.8/851.4	
		$\tilde{\nu}$ (Rh^{18}O_2)	851.3	861.1/849.9		812.5/811.3	
		$\Delta\tilde{\nu}$	39.3	49.0/47.8		39.3/40.1	
	ORhO sym. str. (a')	$\tilde{\nu}$ (Rh^{16}O_2)	837.7	866.5/854.1	21	867.5/859.9	
		$\tilde{\nu}$ (Rh^{18}O_2)	792.1	826.5/815.2		821.1/814.4	
		$\Delta\tilde{\nu}$	45.6	40.0/38.9		46.4/45.5	
$[(\eta^2\text{-O}_2)\text{RhO}_2]$	O–O str. (a_1)	$\tilde{\nu}$ (Rh^{16}O_2)	928.6	1,019.1/976.6	60	968.4/956.4	[24]
		$\tilde{\nu}$ (Rh^{18}O_2)	878.7	962.2/931.2		914.3/901.3	
		$\Delta\tilde{\nu}$	49.9	56.9/45.4		54.1/55.1	
	ORhO sym. str. (a_1)	$\tilde{\nu}$ (Rh^{16}O_2)	865.0	951.0/936.6	10	908.5/897.3	
		$\tilde{\nu}$ (Rh^{18}O_2)	820.3	900.6/88.1		861.2/852.2	
		$\Delta\tilde{\nu}$	44.7	50.4/48.8		47.3/45.1	
	ORhO antisym. str. (b_1)	$\tilde{\nu}$ (Rh^{16}O_2)	831.1	874.6/863.6	100	851.6/844.4	
		$\tilde{\nu}$ (Rh^{18}O_2)	792.1	833.1/823.1		811.0/804.8	
		$\Delta\tilde{\nu}$	39.0	41.5/40.5		40.6/39.6	
RhO ₄	ORhO stretch (e)	$\tilde{\nu}$ (Rh^{16}O_2)	–	912.9/891.0	100	881.5/856.5	
		$\tilde{\nu}$ (Rh^{18}O_2)	–	887.4/849.5		840.1/816.5	
		$\Delta\tilde{\nu}$	–	42.9/41.5		41.4/40.0	
	ORhO stretch (b_2)	$\tilde{\nu}$ (Rh^{16}O_2)	–	882.4/880.5	52	843.1/842.4	
		$\tilde{\nu}$ (Rh^{18}O_2)	–	839.0/837.6		801.6/801.5	
		$\Delta\tilde{\nu}$	–	43.3/42.9		41.5/40.9	

^a Harmonic/anharmonic values; ^b B3LYP; ^c BP86**Table 5** Experimental (in argon matrix) and calculated wavenumbers and isotopic shifts for both $[\text{Rh}(\eta^2\text{-O}_2)_2]$ isomers; all values in cm^{-1}

Molecule	Mode		Exp.	Calc. ^{a,b}	Rel. Int. ^b	Calc. ^{a,c}	Ref.
$[\text{Rh}(\eta^2\text{-O}_2)_2]$ $^2\text{B}_1$	O–O antisym. str. (b_2)	$\tilde{\nu}$ (Rh^{16}O_2)	922.3	993.0/981.9	100	1,018.4/994.6	This paper
		$\tilde{\nu}$ (Rh^{18}O_2)	873.3	938.6/928.8		962.4/945.2	
		$\Delta\tilde{\nu}$	49.0	54.4/53.1		56.3/49.4	
	Rh–(O ₂) ₂ antisym. str. (b_2)	$\tilde{\nu}$ (Rh^{16}O_2)	551.8	606.7/591.3	4	585.5/572.0	
		$\tilde{\nu}$ (Rh^{18}O_2)	531.3	584.0/569.7		563.9/550.9	
		$\Delta\tilde{\nu}$	20.5	22.7/21.6		21.6/21.2	
$[\text{Rh}(\eta^2\text{-O}_2)_2]$ $^4\text{B}_{1u}$	O–O antisym. str. (b_{1u})	$\tilde{\nu}$ (Rh^{16}O_2)	1,048.4	1,172.5/1,156.0	100	1,061.3/1,056.3 ^d	[26]
		$\tilde{\nu}$ (Rh^{18}O_2)	990.3	1,105.5/1,092.9		1,001.1/997.9	
		$\Delta\tilde{\nu}$	58.1	67.0/63.1		60.2/58.4	

^a Harmonic/anharmonic values; ^b B3LYP; ^c BP86; ^d C_{2v} symmetry with BP86

Table 6 Experimental (in argon matrix) and calculated wavenumbers and isotopic shifts for RhO_2 , RhO_2^- and $[\text{Rh}(\eta^2\text{-O}_2)]$; all values in cm^{-1}

Molecule	Mode		Exp.	Calc. ^{a,b}	Rel. Int. ^b	Calc. ^{a,c}	Ref.
RhO_2	ORhO antisym. str. (b_2)	$\tilde{\nu}$ (Rh^{16}O_2)	899.9	986.0/974.9	100	962.3/953.1	[24]
		$\tilde{\nu}$ (Rh^{18}O_2)	861.1	942.8/932.7		920.2/911.9	
		$\Delta\tilde{\nu}$	38.8	43.2/42.2		42.1/41.2	
RhO_2^-	ORhO antisym. str. (b_2)	$\tilde{\nu}$ (Rh^{16}O_2)	893.6	948.9/942.2	100	921.9/909.4	[25]
		$\tilde{\nu}$ (Rh^{18}O_2)	855.3	907.6/901.5		881.7/869.9	
		$\Delta\tilde{\nu}$	38.3	41.3/40.7		40.2/39.5	
$[\text{Rh}(\eta^2\text{-O}_2)]$	O–O str. (a_1)	$\tilde{\nu}$ (Rh^{16}O_2)	959.5	1,072.1/1,016.2	100	1,064.7/1,037.5	[26]
		$\tilde{\nu}$ (Rh^{18}O_2)	907.9	1,011.2/967.9		1,004.0/964.0	
		$\Delta\tilde{\nu}$	51.6	60.9/48.3		60.7/73.5	

^a Harmonic/anharmonic values; ^b B3LYP; ^c BP86

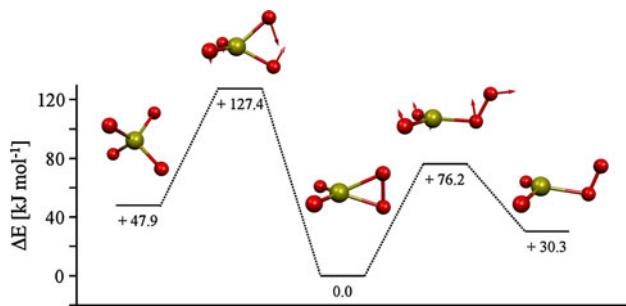


Fig. 8 Computed potential energy diagram (B3LYP results) of the isomers of RhO_4 . Values are energies in kJ mol^{-1} relative to the most stable $[(\eta^2\text{-O}_2)\text{RhO}_2]$ isomer. The arrows at the transition state structure indicate the directions of the force constants of the imaginary mode (arrow scale factor 0.25)

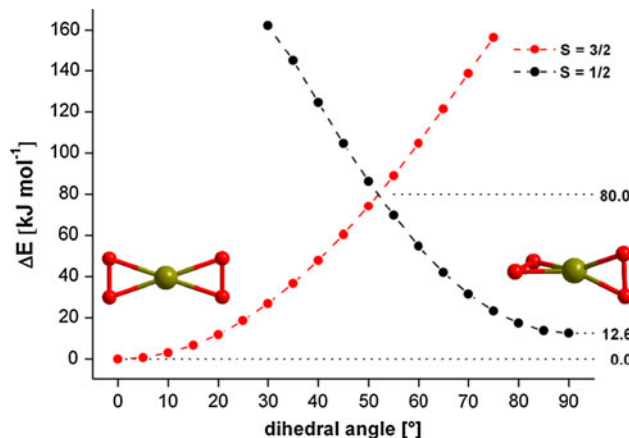


Fig. 9 Relaxed potential energy scan of the doublet and quartet states of $[\text{Rh}(\eta^2\text{-O}_2)_2]$; the potential energies are plotted as a function of the dihedral angle between the two dioxygen groups in an increment of 5°

Fig. 7. This outcome is in agreement with the recently experimental and quantum chemically characterized heavier homologue of IrO_4 [8] and would represent the formal oxidation state VIII of Rh. Thermochemical calculations at DFT and coupled-cluster level show the concerted O_2 elimination $\text{RhO}_4 \rightarrow \text{RhO}_2 + \text{O}_2$ to be exothermic by

−35.2 and −0.6 kJ/mol, respectively. Smaller basis sets tend to overestimate the stability of the higher oxidation states, see Table 3. Furthermore, the RhO_4 isomer is computed to be 47.9 kJ/mol higher in energy than the side-on bonded $[(\eta^2\text{-O}_2)\text{RhO}_2]$ isomer, see Fig. 8. This shows that RhO_4 in oxidation state VIII most likely undergoes an internal reductive bond formation which corresponds to the oxidation state VI of Rh in $[(\eta^2\text{-O}_2)\text{RhO}_2]$, see Table 3. The reaction path for forming the RhO_4 via $[(\eta^2\text{-O}_2)\text{RhO}_2] \rightarrow \text{TS} \rightarrow \text{RhO}_4$ is kinetically protected by a relative high barrier of 127.4 kJ/mol at B3LYP level which one has to overcome for experimental preparation. However, this barrier vice versa (79.5 kJ/mol, see Fig. 8) can in principle stabilize RhO_4 if it is formed. The corresponding TS structure shows approximatively C_{2v} symmetry with two elongated oxygen bonds having an average length of 182.9 pm, see Fig. 8. As no experimental IR band in the matrix isolation experiment could be assigned to this RhO_4 species, the case of rhodium contrasts with our recent results for iridium oxides [8].

Structure optimizations and frequency (harmonic and anharmonic) calculations of the lower rhodium oxides RhO_2 , $[\text{RhO}_2]^-$ and $[\text{Rh}(\eta^2\text{-O}_2)]$ have been performed as well, see Fig. 7 and Table 6. Both rhodium dioxide species RhO_2 and $[\text{RhO}_2]^-$ are not linear with a bending angle of 158.4 and 163.9°, respectively. The computed bond length of 167.6 pm of the RhO_2 molecule is the shortest found for all investigated rhodium oxides in this work. The $[\text{Rh}(\eta^2\text{-O}_2)]$ species shows C_{2v} symmetry with its O–O bond length of 133.3 pm which lies between the peroxy and superoxo complexes f and g in Fig. 7.

4 Conclusions

As observed in previous experiments [24, 26], ground-state rhodium atoms react with O_2 to form the $[\text{Rh}(\eta^2\text{-O}_2)]$ complex while the formation of rhodium dioxide requires

excited rhodium atoms. Further, sample annealing allows the spontaneous formation of the $[(\eta^1\text{-O}_2)\text{RhO}_2]$ complex from RhO_2 and O_2 , for which negligible activation energy is needed. The end-on bonded $[(\eta^1\text{-O}_2)\text{RhO}_2]$ complex can be converted to the $[(\eta^2\text{-O}_2)\text{RhO}_2]$ complex with side-on bonded O_2 molecule via infrared irradiation, and vice versa, under near-infrared irradiation. This species is also computed to be the lowest in energy of all RhO_4 isomers.

Different from the iridium case, rhodium tetroxide is not produced on further photolysis with high-energy photons, suggesting the RhO_4 molecule to be less stable than the heavier iridium analogue in solid matrices. This experimental finding is in agreement with our calculations: RhO_4 is 47.9 kJ/mol higher in energy than its $[(\eta^2\text{-O}_2)\text{RhO}_2]$ isomer which is in contrast with the iridium tetroxide isomers where the IrO_4 isomer was found to be the lowest in energy. The internal reduction path $\text{RhO}_4 \rightarrow [(\eta^2\text{-O}_2)\text{RhO}_2]$ is kinetically hindered by a barrier of only 79.5 kJ/mol at B3LYP level. Nevertheless, the oxidation state VI is highest observed for rhodium. Recent matrix isolation studies on iron and cobalt tetroxide molecules revealed that both the end-on $[(\eta^1\text{-O}_2)\text{MO}_2]$ and side-on bonded $[(\eta^2\text{-O}_2)\text{MO}_2]$ ($\text{M} = \text{Fe}, \text{Co}$) complexes were stable and interconvertible, but no evidence was found for the formation of the tetroxide molecules with the metal centre in the VIII oxidation state [31, 32]. It seems that light transition metal oxides with high oxidation state (higher than VI) are not stable enough to be trapped in solid matrices.

In addition to the rhodium dioxide–dioxygen complexes, two interconvertible $[\text{Rh}(\eta^2\text{-O}_2)_2]$ complexes are also produced when the sample was annealed. Infrared irradiation induced the formation of the superoxo $[\text{Rh}(\eta^2\text{-O}_2)_2]$ complex (A), and the peroxy $[\text{Rh}(\eta^2\text{-O}_2)_2]$ complex (B) is reproduced when visible irradiation was used. Complex B is 12.6 kJ/mol higher in energy, and a relaxed potential energy scan at B3LYP level indicates a barrier of approximately 80 kJ/mol for the interconversion.

Acknowledgments The authors are grateful to I. Krossing and M. Kaupp for kindly providing computational resources. M.Z. thanks the National Basics Research Program of China (2007CB815203) and NSFC (20933003) for financial support. S.R. thanks the Fonds der Chemischen Industrie, the DFG and the Alexander von Humboldt Foundation for financial support. T.S. thanks the Institut für Analytische und Anorganische Chemie for financial support.

References

- Ruff O, Vidic E (1924) Z Anorg Allgem Chem 136:49
- Pley M, Wickleder MS (2005) J Solid State Chem 178:3206
- Bailey AJ, Bhowon MG, Griffith WP, Shoair AGF, White AJP, Williams DJ (1997) J Chem Soc Dalton Trans 3245–3250
- Jewiss HC, Levason W, Tajik M, Webster M, Walker NPC (1985) J Chem Soc Dalton Trans 199–203
- Holleman AF, Wiberg E (2007) Lehrbuch der Anorganischen Chemie. Walter de Gruyter, Berlin
- Riedel S, Kaupp M (2009) Coord Chem Rev 253:606
- Düllmann CE, Bruchle W, Dressler R, Eberhardt K, Eichler B, Eichler R, Gaggeler HW, Ginter TN, Glaus F, Gregorich KE, Hoffman DC, Jager E, Jost DT, Kirbach UW, Lee DM, Nitsche H, Patin JB, Pershina V, Piguet D, Qin Z, Schadel M, Schausten B, Schimpf E, Schott HJ, Soverna S, Sudowe R, Thorle P, Timokhin SN, Trautmann N, Turler A, Vahle A, Wirth G, Yakushev AB, Zielinski PM (2002) Nature 418:859
- Gong Y, Zhou M, Kaupp M, Riedel S (2009) Angew Chem Int Ed 48:7879
- Himmel D, Knapp C, Patzschke M, Riedel S (2010) Chem Phys Chem 11:865
- Wang G, Zhou M (2008) Int Rev Phys Chem 27:1
- Becke AD (1993) J Chem Phys 98:5648
- Dunning TH Jr (1989) J Chem Phys 90:1007
- Peterson Kirk A, Figgen D, Dolg M, Stoll H (2007) J Chem Phys 126:124101
- Frisch MJ, Trucks GW, Schlegel HB, Scuseria GE, Robb MA, Cheeseman JR, Montgomery JA, Vreven JT, Kudin KN, Burant JC, Millam JM, Iyengar SS, Tomasi J, Barone V, Mennucci B, Cossi M, Scalmani G, Rega N, Petersson GA, Nakatsuji H, Hada M, Ehara M, Toyota K, Fukuda R, Hasegawa J, Ishida M, Nakajima T, Honda Y, Kitao O, Nakai H, Klene M, Li X, Knox JE, Hratchian HP, Cross JB, Adamo C, Jaramillo J, Gomperts R, Stratmann RE, Yazyev O, Austin AJ, Cammi R, Pomelli C, Ochterski JW, Ayala PY, Morokuma K, Voth GA, Salvador P, Dannenberg JJ, Zakrzewski VG, Dapprich S, Daniels AD, Strain MC, Farkas O, Malick DK, Rabuck AD, Raghavachari K, Foresman JB, Ortiz JV, Cui Q, Baboul AG, Clifford S, Cioslowski J, Stefanov BB, Liu G, Liashenko A, Piskorz P, Komaromi I, Martin RL, Fox DJ, Keith T, Al-Laham MA, Peng CY, Nanayakkara A, Challacombe M, Gill PMW, Johnson B, Chen W, Wong MW, Gonzalez C, Pople JA (2003) Revision B.04 ed. Pittsburgh PA
- Werner H-J, Knowles PJ, Lindh R, Manby FR, Schütz M, Celani P, Korona T, Rauhut G, Amos RD, Bernhardsson A, Berning A, Cooper DL, Deegan MJO, Dobbyn AJ, Eckert F, Hampel C, Hetzer G, Lloyd AW, McNicholas SJ, Meyer W, Mura ME, Nicklaß A, Palmieri P, Pitzer R, Schumann U, Stoll H, Stone AJ, Tarroni R, Thorsteinsson T (2006) MOLPRO 2006.1 ed. Birmingham, UK
- Riedel S, Straka M, Kaupp M (2004) Phys Chem Chem Phys 6:1122
- Riedel S, Kaupp M (2006) Angew Chem Int Ed 45:3708
- Riedel S, Kaupp M (2006) Inorg Chem 45:1228
- Himmel D, Riedel S (2007) Inorg Chem 46:5338
- Riedel S (2007) J Fluorine Chem 128:938
- Lee TJ, Taylor PR (1989) Int J Quantum Chem 23:199
- Li ZH, Gong Y, Fan K, Zhou M (2008) J Phys Chem A 112:13641
- Chertihi GV, Andrews L (1998) J Chem Phys 108:6404
- Citra A, Andrews L (1999) J Phys Chem A 103:4845
- Gong Y, Zhou M (2009) J Phys Chem A 113:4990
- Yang R, Gong Y, Zhou H, Zhou M (2007) J Phys Chem A 111:64
- Jacox ME (1994) Chem Phys 189:149
- Gong Y, Zhou M, Andrews L (2009) Chem Rev 109:6765
- Swart M (2008) J Chem Theory Comput 4:2057
- Rong C, Lian S, Yin D, Shen B, Zhong A, Bartolotti L, Liu S (2006) J Chem Phys 125:174102/1
- Gong Y, Zhou M, Andrews L (2007) J Phys Chem A 111:12001
- Danset D, Alikhani ME, Manceron L (2005) J Phys Chem A 109:105